

# Supplementary Material: First measurement of $\eta$ production in neutrino interactions on argon with MicroBooNE

## I. SHOWER ENERGY-SCALE CALIBRATION

Diphoton pairs from background  $\pi^0$  candidates can be isolated by requiring the reconstructed diphoton invariant mass be consistent with the  $\pi^0$  mass. The invariant mass is defined as

$$M_{\gamma\gamma} = \sqrt{2E_1E_2(1 - \cos\theta_{\gamma\gamma})}, \quad (1)$$

with  $E_1$  and  $E_2$  the energy of the leading and sub-leading photons, respectively, and  $\theta_{\gamma\gamma}$  the opening angle between the two photons. To select  $\pi^0$  candidates a requirement that  $M_{\gamma\gamma}$  be less than  $250 \text{ MeV}/c^2$  is imposed. The sample of events, referred to as the “ $\pi^0$ -sideband”, can be used to further validate the EM shower energy-scale calibration. The shape-only comparison of the data/MC agreement in the invariant diphoton mass for this sample of events is shown in Fig. 1. The background-subtracted  $M_{\gamma\gamma}$  distribution is fit to a Gaussian plus low-end exponential tail distribution to obtain a fit for the invariant mass of  $128 \text{ MeV}$  with a Gaussian width of  $31 \text{ MeV}$ . The energy of all EM showers is increased by  $5.2\%$  to correct for the difference between the measured and actual  $\pi^0$  mass. The same  $\pi^0$ -sideband will later be used to constrain  $\pi^0$  backgrounds in the cross section extraction.

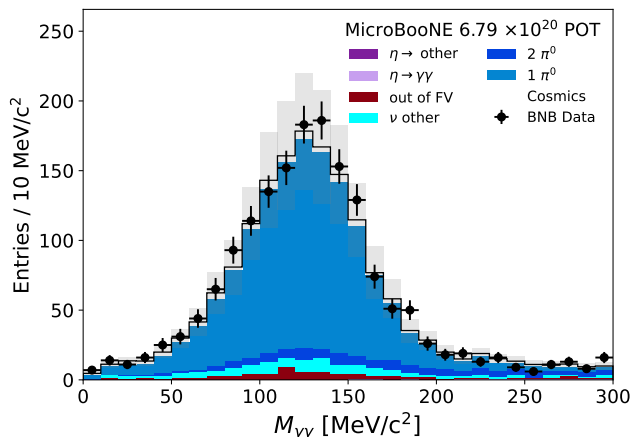


FIG. 1. Shape-only diphoton invariant mass from candidate  $\pi^0$  events.

## II. $\pi^0$ BACKGROUND CONSTRAINT.

Backgrounds to the analysis are primarily due to events with final-state  $\pi^0$ , with multi- $\pi^0$  events making the dominant background contribution. The background rate for  $1\pi^0$  and multi- $\pi^0$  events are constrained via in-situ measurement in sideband channels. For background events with a single final-state  $\pi^0$ , the  $\pi^0$ -sideband described above is used. For multi- $\pi^0$  events, the same  $\pi^0$ -sideband selection is applied but requiring four rather than two reconstructed showers greater than  $50 \text{ MeV}$  in energy and allowing  $M_{\gamma\gamma} < 700 \text{ MeV}$ . The constraint is carried out as a one-bin measurement. Before proceeding with the constraint itself, the level of agreement between data and the prediction is quantified. Figure 2 shows the one-bin measurements for the  $1\pi^0$  and  $2\pi^0$  sidebands, respectively. In both, the data is found to be lower than the prediction. The gray bands denote the systematic uncertainty on the predicted number of events. For the  $1\pi^0$  sideband we observe  $1634 \pm 40$  events (the uncertainty is on the data statistics) with a predicted rate of  $2020 \pm 519$  (the uncertainty is the total systematic error on the prediction). For the  $2\pi^0$  sideband the observed and predicted events, with uncertainties, are  $59 \pm 8$  and  $77 \pm 27$ . Both distributions show the data close to the  $1\sigma$  lower variation on the prediction. The model is able to reproduce the data within uncertainties, leading to a  $\chi^2$  of  $0.66$  and  $0.87$ , respectively.

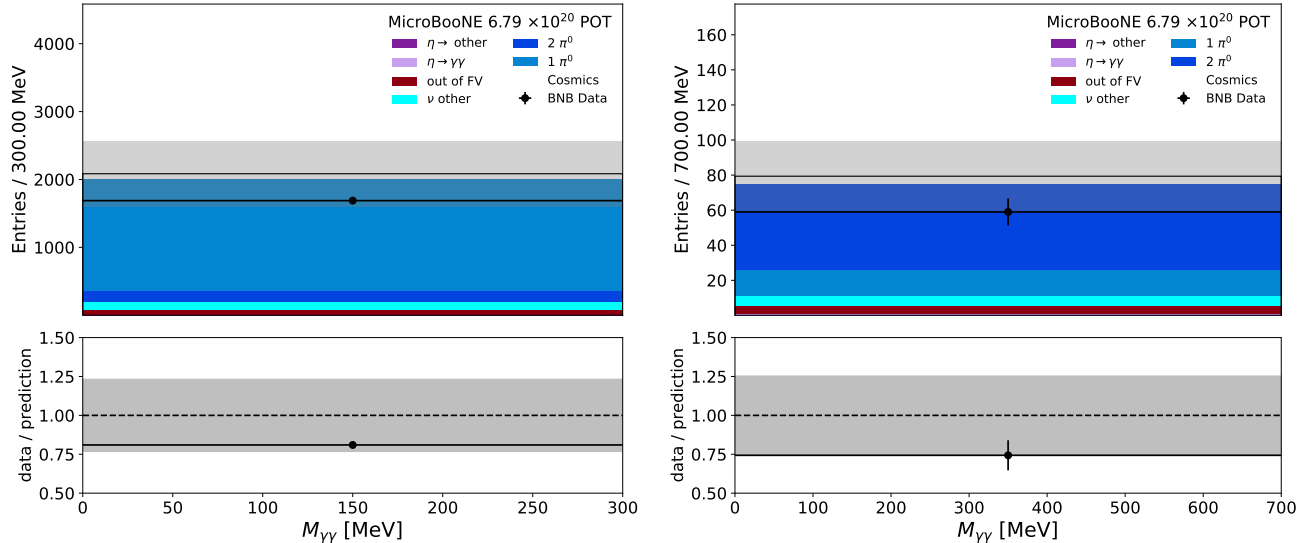


FIG. 2. Left:  $1\pi^0$  sideband. Right:  $2\pi^0$  sideband. The  $\chi^2/1$  degree of freedom is 0.66 and 0.87, respectively.

Backgrounds are constrained through the Conditional Covariance formalism [1] accounting for correlations between the sideband constraint sample and signal region. This method is used to update the predicted background rate and its uncertainty in the signal region through the expressions below:

$$N_{MC}^{S,constrained} = N_{MC}^S + \frac{\sigma^{cov}}{(\sigma^B)^2} \times (N_{data}^B - N_{MC}^B), \quad (2)$$

$$(\sigma^{S,constrained})^2 = (\sigma^S)^2 - \frac{(\sigma^{cov})^2}{(\sigma^B)^2}. \quad (3)$$

$N_{MC}^{S,B}$  denote the predicted number of background events ( $1\pi^0$  or  $2\pi^0$ , depending on the channel being constrained) in the signal (S) region and background constraint (B) region.  $N_{data}^B$  is the number of observed events in the sideband (after subtracting backgrounds from other categories not being constrained).  $\sigma^B$  and  $\sigma^S$  denote the total uncertainty (systematic and statistical) on the background events being constrained in the background constraint and signal regions, respectively. Finally,  $\sigma^{cov}$  refers to the covariance between background events measured in the constraint sideband and signal region. Given that both sideband and signal regions are single-bin measurements, the covariance for  $1\pi^0$  and multi- $\pi^0$  sidebands and their expected rates in the signal region is given by a single number which is measured by calculating the variation in the event rates according to the formula

$$\sigma^{cov}(\text{signal, sideband}) = \frac{1}{N} \sum_{i=1}^{i=N} [n_i(\text{signal}) - n_{CV}(\text{signal})] \times [n_i(\text{sideband}) - n_{CV}(\text{sideband})] \quad (4)$$

where  $n$  denotes the number of expected events,  $i$  denotes a given systematic variation universe, CV the central value expectation for the simulation, and  $N$  the systematic variations contributed by flux, cross section, and detector modeling uncertainties. The magnitude of the correlation between signal sample and the  $1\pi^0$  and  $2\pi^0$  sidebands are found to be 0.73 and 0.79, respectively. This leads to a constrained background rate in the signal region of 13.2  $1\pi^0$  and 24.6 multi- $\pi^0$  events, which represents a scaling of 0.835 and 0.795 respectively for the two channels. Table I summarizes the outcome of the conditional constraint procedure, and Fig. 3 shows the predicted event rates in the signal region before (left) and after (right) background constraint.

### III. $\eta$ SELECTION

The last step of the selection includes cuts on the kinematics of di-photon events in order to further discriminate  $\pi^0$  background from  $\eta$  signal events. Before describing the final kinematic cuts themselves, a new variable is introduced

	before constraint		after constraint	
background	prediction	uncertainty	prediction	uncertainty
$1\pi^0$	15.8	4.1	13.2	2.6
$2\pi^0$	31.0	7.8	22.6	4.4

TABLE I. Predicted background events in the signal region and their uncertainty before and after constraint.

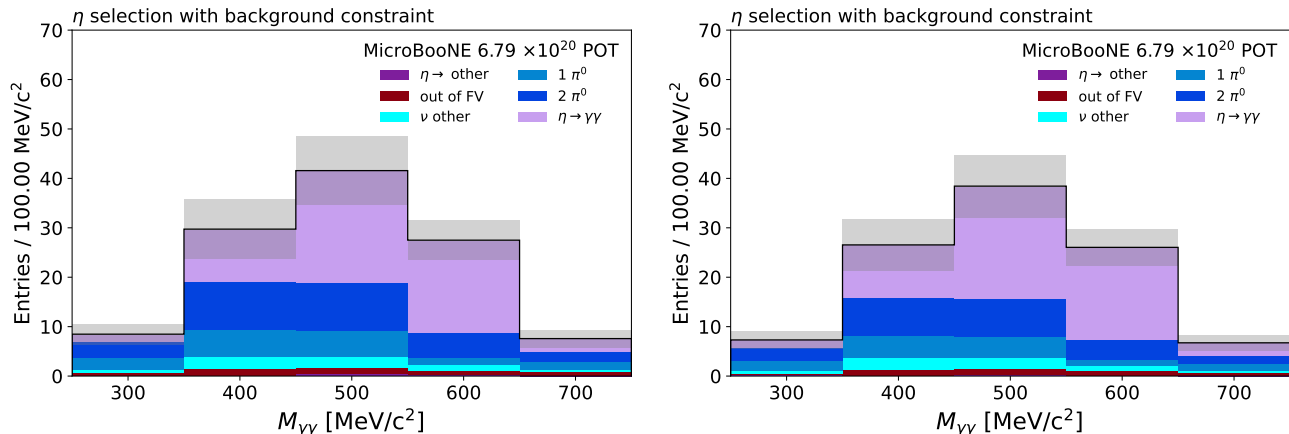


FIG. 3. Prediction for the event rate in the signal region before (left) and after (right) the sideband constraint applied to  $1$  and  $2\pi^0$  events.

in the analysis:  $M_{\max}$ . This reconstructed variable denotes the maximum mass a particle with a given its decay two two photons. This variable is defined as  $M_{\max}$  and is computed as

$$M_{\max} = (E_1 + E_2) \sqrt{\frac{1}{2} (1 - \cos \theta_{\gamma\gamma})}, \quad (5)$$

with  $E_1$  and  $E_2$  the energy of the two photons and  $\theta_{\gamma\gamma}$  the angle between them in the lab frame. The derivation for why Eq. 5 gives the maximum allowed mass for a particle decaying to two photons is given below. Given a particle of mass  $M^*$  decaying to two photons of energy  $E_1$  and  $E_2$  and opening angle  $\theta_{\gamma\gamma}$ , the invariant mass of their decay is given by Eq. 1. We can express  $E_1$  as  $(M^* - E_2)$ , and substituting we obtain

$$M^* = \sqrt{2 (M^* - E_2) E_2 (1 - \cos \theta_{\gamma\gamma})}. \quad (6)$$

Comparing equations 5 and 6 and cancelling out the common term  $1 - \cos \theta_{\gamma\gamma}$ , we find that

$$2 (M^* - E_2) E_2 \leq \frac{M^*}{2}. \quad (7)$$

holds true for all values of  $E_2 < M^*$ . The relation becomes an identity when  $E_2$  is equal to  $M^*/2$ . Therefore, Equation 5 gives the expression for the maximum possible mass of a particle decaying to two photons of energy  $E_1$  and  $E_2$  with opening angle  $\theta_{\gamma\gamma}$ .

To further reject background events with final-state  $\pi^0$  particles, two cuts on the kinematics of the diphoton pair are implemented:  $\cos \theta_{\gamma\gamma} < 0.5$  and  $M_{\max} > 400 \text{ MeV}/c^2$ . The efficacy of this cut can be seen in Fig. 4. The plot shows the correlation between the sum of the shower energy and the diphoton opening angle for both  $\eta$  and  $\pi^0$  decays. The black and blue dotted lines trace the value of  $M_{\max}$  as a function of the true minimum opening angle kinematically allowed by the decay. The red points show the correlation between the two variables for reconstructed  $\eta \rightarrow \gamma\gamma$  decays from the simulation, while the tiled 2D histogram shows the same reconstructed distribution for true  $\pi^0 \rightarrow \gamma\gamma$  events. The figure shows both how  $\pi^0$  decays are much more boosted due to the lower  $\pi^0$  mass for equal energy photon pairs. This motivates the cut at  $\cos \theta_{\gamma\gamma} < 0.5$  which removes a very small amount of signal  $\eta$  candidates. The strong

separation in 2D between the two distributions further justifies the cut on  $M_{\max}$  which can nicely separate the two populations as indicated by the dotted curves that trace the profile of  $M_{\max}$  for the values of  $M_{\max}$  equal to the  $\pi^0$  and  $\eta$  mass.

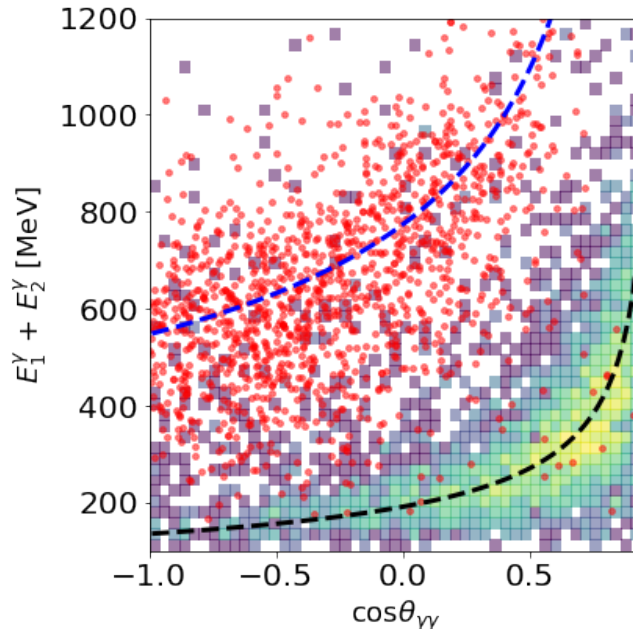


FIG. 4. Discrimination of  $\eta$  and  $\pi^0$  events decaying to two photons based on diphoton kinematics. The black and blue dotted lines traces the value of  $M_{\max}$  as a function of the true minimum opening angle kinematically allowed by the decay. The red points show the correlation between the two variables for reconstructed  $\eta \rightarrow \gamma\gamma$  decays from the simulation, while the tiled 2D histogram shows the same reconstructed distribution for true  $\pi^0 \rightarrow \gamma\gamma$  events from the simulation.

Figures 5 and 6 show the distributions of  $M_{\max}$  and  $\cos\theta_{\gamma\gamma}$  before cuts on these variables are applied. The plots show the clear separation between signal  $\eta$  events in purple and background. Cut values for these variables were determined by studying the prediction only distribution from simulation without information on the distribution of data events.

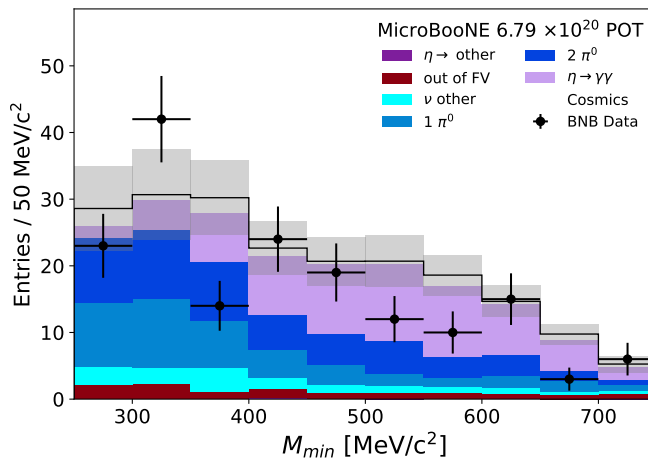


FIG. 5. Distribution for  $M_{\max}$  before the final selection cuts on this variable and  $\cos\theta_{\gamma\gamma}$  are applied.

Figure 7 shows the efficiency for selecting  $\eta$  candidates for the different selection stages in the analysis. At every step in the selection, the efficiency is flat with respect to the  $\eta$  particle's energy, up to 1 GeV. After implementing a

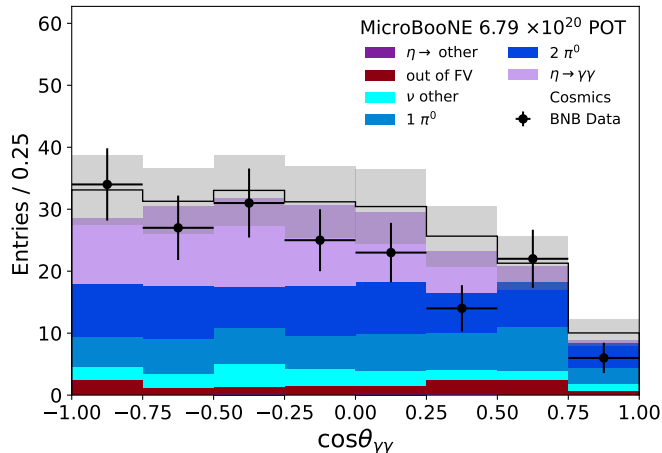


FIG. 6. Distribution for  $\cos\theta_{\gamma\gamma}$  before the final selection cuts on this variable and  $M_{\max}$  are applied.

requirement that two reconstructed showers with greater than 50 MeV of energy each are reconstructed in the event, the efficiency drops to 40%, a consequence largely of reconstruction inefficiencies in events with complex topologies with multiple EM showers. Further quality cuts on the reconstructed showers bring the efficiency to 20%, while the rejection of  $\pi^0$  candidates through the cut  $M_{\gamma\gamma} > 250$  MeV has negligible impact on the efficiency. The final selection requirement that  $M_{\max} > 400$  MeV and  $\cos\theta_{\gamma\gamma} < 0.5$  decreases the efficiency to 13.6% without, however, energy-dependence up to 1 GeV.

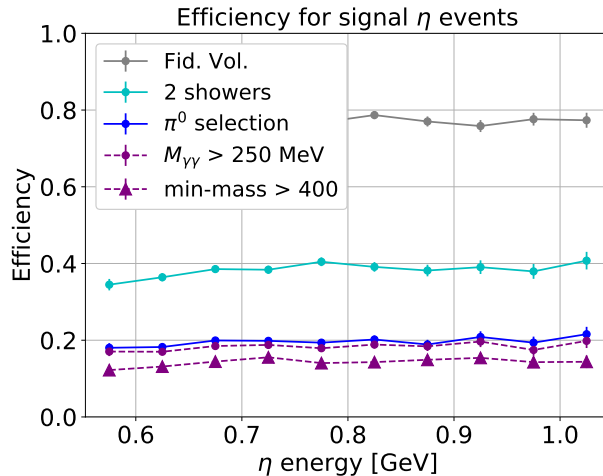


FIG. 7.  $\eta$  selection efficiency. The grey curve labeled as “Fid. Vol.” denotes the efficiency for identifying a neutrino interaction which match the signal topology within the MicroBooNE fiducial volume.

#### IV. EXTRACTED CROSS SECTION

Figure 8 shows a comparison of the extracted flux-integrated cross section to that obtained through truth-studies of different generators. The result here is presented for inclusive  $\eta$  production after having corrected for the branching ratio for  $\eta \rightarrow 2\gamma$  of  $39.41\% \pm 0.20\%$  [2]. Note that the very high precision with which this branching ratio is measured does not introduce a noticeable increase in the uncertainty in the extracted cross section. The extracted cross section of  $3.22 \pm 0.84$  (stat.)  $\pm 0.86$  (syst.)  $10^{-41} \text{cm}^2/\text{nucleon}$ . The measurement from NEUT [3] of  $1.19 \cdot 10^{-40} \text{cm}^2/\text{nucleon}$ ,

found to be significantly larger than the extracted cross section, falls out of range of the plot above.

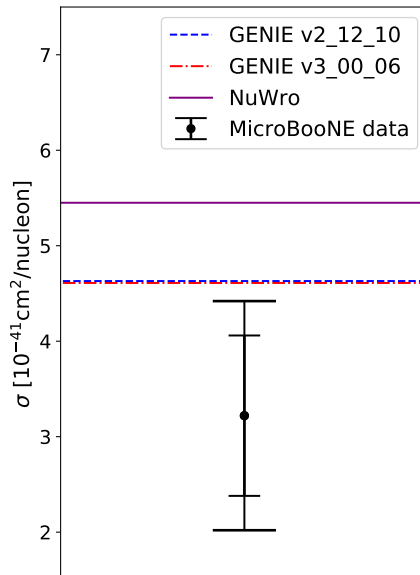


FIG. 8. Comparison of extracted cross section from data to predictions.

The limited nucleon excitations that decay with sizeable branching ratios to  $\eta$  particles leads to the observation that selecting  $\eta$  candidates is a powerful way to tag specific resonance states. In particular, nearly 90% of  $\eta$  particles produced in neutrino interactions from the BNB in MicroBooNE are predicted to originate from the decay of the  $N(1535)$  excitation. Figure 9 shows a truth-level distribution of the hadronic invariant mass  $W$  from the GENIE v3.0.6 G18\_10a\_02\_11a generator prediction for MicroBooNE's neutrino flux for resonant interactions separated by each resonant state.  $\Delta(1232)$  dominates the resonant production. The contribution from the  $N(1535)$ , subleading with respect to the  $\Delta$ , is significant compared to other less relevant resonances. While the  $N(1520)$  has a comparable contribution to the event rate, its branching ratio to  $\eta$  mesons is negligible. The clear separation in the invariant mass due to the excitation is something that was observed with the  $\eta$  candidates from the analysis, as presented in the main results for the analysis.

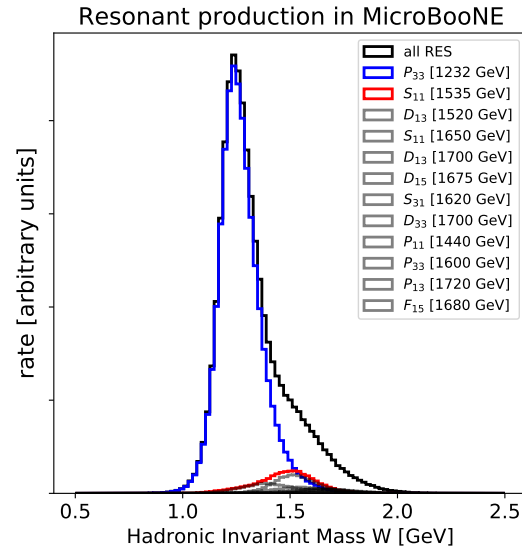


FIG. 9. Invariant mass of the hadronic system for true RES interactions as modeled in MicroBooNE. The resonance labeled as  $P_{33}$  (blue) corresponds to the  $\Delta(1232)$ , and  $S_{11}$  (red) corresponds to  $N(1535)$ . The state  $D_{13}$  corresponds to the  $N(1520)$  resonance. The  $\Delta(1232)$  contribution dominates the distribution making it challenging to study the sizeable contribution of higher mass resonances.

- 
- [1] Morris L. Eaton, *Multivariate statistics: a vector space approach* (Wiley, New York, 1983) pp. 116–117.  
 [2] R. L. Workman and Others (Particle Data Group), “Review of Particle Physics,” PTEP **2022**, 083C01 (2022).  
 [3] Yoshinari Hayato, “A neutrino interaction simulation program library NEUT,” Acta Phys. Polon. B **40**, 2477–2489 (2009).